

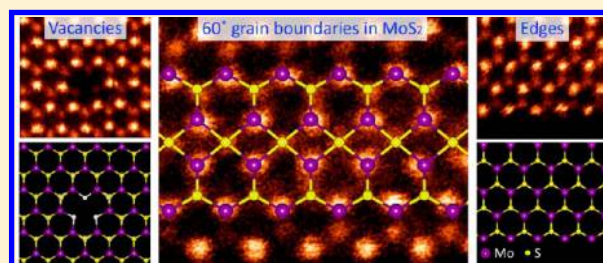
## Intrinsic Structural Defects in Monolayer Molybdenum Disulfide

Wu Zhou,<sup>\*,†,‡</sup> Xiaolong Zou,<sup>§</sup> Sina Najmaei,<sup>§</sup> Zheng Liu,<sup>§</sup> Yumeng Shi,<sup>||</sup> Jing Kong,<sup>||</sup> Jun Lou,<sup>§</sup> Pulickel M. Ajayan,<sup>§</sup> Boris I. Yakobson,<sup>§</sup> and Juan-Carlos Idrobo<sup>†</sup><sup>†</sup>Materials Science and Technology Division, Oak Ridge National Laboratory, Oak Ridge, Tennessee 37831, United States<sup>‡</sup>Department of Physics and Astronomy, Vanderbilt University, Nashville, Tennessee 37235, United States<sup>§</sup>Department of Mechanical Engineering and Materials Science, Rice University, Houston, Texas 77005, United States<sup>||</sup>Department of Electrical Engineering and Computer Sciences, Massachusetts Institute of Technology, Cambridge, Massachusetts 02139, United States

## S Supporting Information

**ABSTRACT:** Monolayer molybdenum disulfide (MoS<sub>2</sub>) is a two-dimensional direct band gap semiconductor with unique mechanical, electronic, optical, and chemical properties that can be utilized for novel nanoelectronics and optoelectronics devices. The performance of these devices strongly depends on the quality and defect morphology of the MoS<sub>2</sub> layers. Here we provide a systematic study of intrinsic structural defects in chemical vapor phase grown monolayer MoS<sub>2</sub>, including point defects, dislocations, grain boundaries, and edges, via direct atomic resolution imaging, and explore their energy landscape and electronic properties using first-principles calculations. A rich variety of point defects and dislocation cores, distinct from those present in graphene, were observed in MoS<sub>2</sub>. We discover that one-dimensional metallic wires can be created via two different types of 60° grain boundaries consisting of distinct 4-fold ring chains. A new type of edge reconstruction, representing a transition state during growth, was also identified, providing insights into the material growth mechanism. The atomic scale study of structural defects presented here brings new opportunities to tailor the properties of MoS<sub>2</sub> via controlled synthesis and defect engineering.

**KEYWORDS:** Monolayer molybdenum sulfide, point defects, dislocation, grain boundary, edge reconstruction, atomic resolution imaging, first-principles calculations



Monolayer molybdenum disulfide (MoS<sub>2</sub>) is a quasi-two-dimensional (2D) crystal, consisting of two atomic layers of close-packed S atoms separated by one close-packed Mo atomic layer. MoS<sub>2</sub> displays many intriguing physical and chemical properties with a wide range of promising applications.<sup>1–6</sup> In particular, MoS<sub>2</sub> in its monolayer form is a direct bandgap semiconductor,<sup>1</sup> which can be used to produce smaller and more energy efficient field-effect transistors (FETs), integrated logic circuits, photodetectors, and flexible optoelectronic devices.<sup>2–6</sup> For any of these applications to become practical, synthesis of high quality monolayer films with large areas is required. Very recently, it has been shown that synthesis of large films of polycrystalline monolayer MoS<sub>2</sub> could be achieved using chemical vapor deposition (CVD).<sup>7–11</sup> However, as compared to mechanically exfoliated samples, the CVD grown MoS<sub>2</sub> monolayers typically have much lower carrier mobility,<sup>7,10</sup> due to growth process imperfections that induce various structural defects in the material.<sup>12</sup>

It has been well documented that structural defects in graphene, including point defects, grain boundaries (GB), and edges, can have significant influence on the mechanical, optical, thermal, and electrical properties of the material. For example, certain types of GBs have been shown to weaken the

mechanical strength<sup>13</sup> and degrade the electronic performance of graphene.<sup>14,15</sup> On the other hand, structural defects in 2D materials provide exciting opportunities to tailor the local properties creating new functionalities. Examples include the generation of tunable magnetic phases in graphene with vacancies,<sup>16</sup> and local enhancement of optical excitations at graphene edges.<sup>17</sup> Compared to graphene, which only contains one atomic layer of carbon, structural defects in MoS<sub>2</sub> have rarely been explored<sup>11,18–20</sup> due to the increased complexity from the three-dimensional structure and the binary element system involved.

In this article, we provide a systematic study of intrinsic point defects, dislocations, GBs, and edges in high-quality monolayer MoS<sub>2</sub> grown by CVD method,<sup>11</sup> using a combination of direct atomic resolution imaging and first-principles calculations. We report direct observation of various vacancies, as well as antisite defects of Mo and S, and explore their possible influences on the *n*-type conductivity commonly observed in CVD MoS<sub>2</sub> samples. In addition, we explore various GBs with distinct

Received: February 28, 2013

Revised: May 3, 2013

Published: May 9, 2013

dislocation core structures in monolayer MoS<sub>2</sub>. We show that 60° grain boundaries mainly consist of two different types of 4-fold ring chains, either edge sharing or point sharing, and both serve as one-dimensional metallic wires in the 2D semiconducting lattice. A new type of reconstructed edge was also observed, representing a transition state during the growth process.

Figure 1A shows an optical micrograph of the monolayer MoS<sub>2</sub> sample grown on SiO<sub>2</sub> substrate.<sup>11</sup> The triangular-shaped

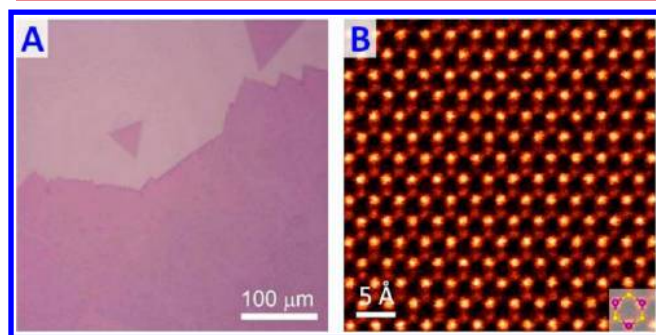


**Figure 1.** CVD growth of highly crystalline monolayer MoS<sub>2</sub>. (A) Optical image of large area CVD MoS<sub>2</sub> atomic layers grown on SiO<sub>2</sub> substrate. (B) Atomic resolution STEM-ADF image from clean monolayer MoS<sub>2</sub> with structural model overlaid. Purple and yellow balls represent Mo and S<sub>2</sub>, respectively.

crystal is primarily single-crystalline monolayer MoS<sub>2</sub> with size of a few tens of micrometers, while the continuous film is polycrystalline with multiple adjacent triangle-shaped crystals.<sup>11</sup> The as-grown film was transferred onto a TEM grid (see Methods in Supporting Information), and the atomic structure of the material was studied using atomic-resolution annular dark field (ADF) imaging on an aberration-corrected scanning transmission electron microscope (STEM). The ADF image intensity is proportional to the number of atomic layers for thin samples, providing an easy and accurate way to measure the thickness of thin samples without the need for image simulation (Supporting Information Figure S1). Moreover, the ADF image intensity is also directly related to the atomic number of the atoms imaged, allowing atom-by-atom chemical identification via quantitative analysis of the image intensity (Supporting Information Figure S2)<sup>21–23</sup> at various defect sites, as it is shown in the following discussion. A typical STEM-ADF image from clean monolayer region is shown in Figure 1B with alternating Mo and S<sub>2</sub> columns arranging into hexagonal rings.

Point defects are inevitable in any material as suggested by the second law of thermodynamics and are particularly noticeable in chemically grown 2D materials due to the imperfection of the growth process. As has been shown for graphene with different combination and reconstruction, there exists an almost infinite number of defects in the 2D lattice;<sup>12</sup> thus, we only focus on the simplest intrinsic defects when the crystal structure is perturbed without the presence of foreign atoms.

Figure 2A shows the STEM-ADF images from six different types of point defects commonly observed in CVD grown monolayer MoS<sub>2</sub>, including monosulfur vacancy ( $V_S$ ), disulfur vacancy ( $V_{S_2}$ ), vacancy complex of Mo and nearby three sulfur ( $V_{MoS_3}$ ), vacancy complex of Mo nearby three disulfur pairs ( $V_{MoS_6}$ ), and antisite defects where a Mo atom substituting a S<sub>2</sub> column ( $Mo_{S_2}$ ) or a S<sub>2</sub> column substituting a Mo atom ( $S_{2Mo}$ ). The atom-by-atom chemical analysis capability of STEM-ADF

imaging enables us to unambiguously identify a monosulfur vacancy from disulfur vacancy, and antisite defects from regular lattice sites, by quantitative analysis of the image intensity (Supporting Information Figure S3).

To explore the energy landscape of the observed point defects, we performed first-principles calculations based on density functional theory (DFT). The optimized defect structures from DFT calculations are shown in Figure 2B, which are in excellent agreement with the experimental STEM images. Specifically, most of the defect structures maintain the 3-fold symmetry, while MoS<sub>2</sub> explicitly breaks the symmetry with Mo locating closer to two of the three nearest-neighbor Mo atoms and at one of the two S layers.

The structural stability of different point defects can be explored through their formation energies. The defect formation energies as a function of S chemical potential, over a wide range of experimental conditions from Mo-rich to S-rich, are plotted in Figure 2C. The slopes of the energy profiles are proportional to the excess/deficit of S atoms in the defects. In the whole range of S chemical potential,  $V_S$  is found to have the lowest formation energy, while  $Mo_{S_2}$  and  $S_{2Mo}$  antisite defects are among the highest formation energies under S-rich and Mo-rich environments, respectively. This is consistent with our experimental observations, where  $V_S$  is frequently observed in all samples, but antisite defects were only occasionally found. Moreover, the formation energy of  $V_{S_2}$  is roughly twice of that of  $V_S$ , suggesting that  $V_S$ 's do not have a strong tendency to combine. The theoretical result is also confirmed by our experiments, where randomly distributed  $V_S$ 's were observed far more frequently than  $V_{S_2}$ 's. This is in sharp contrast to the scenario in graphene, where divacancies are energetically favored over monovacancies.<sup>24,25</sup> Our calculations show that  $V_{Mo}$  has lower formation energy than  $V_{MoS_3}$  over a large S chemical potential range except for under Mo-rich environment. However, once the  $V_{Mo}$  is generated, the S atoms around it become strongly prone to lose with the vacancy formation energy of only 1.1 eV per  $V_S$  even under S-rich condition. That is the reason why we did not observe any  $V_{Mo}$  alone. Most Mo vacancies are present as defect complexes of  $V_{MoS_3}$ . On the other hand, the formation energy for S vacancies next to  $V_{MoS_3}$  is similar to that of  $V_S$ ; hence,  $V_{MoS_6}$  complexes were only observed occasionally, presumably due to slight electron beam irradiation damage. Moreover,  $V_{MoS_2}$ , containing a  $V_{Mo}$  and  $V_{S_2}$  pair, has never been observed in our experiment due to its higher formation energy than  $V_{MoS_3}$ .

The effects of the observed point defects on the electronic properties of MoS<sub>2</sub> were also studied. We plot the in-gap defect levels schematically for three types of defects:  $V_S$ ,  $V_{S_2}$ , and  $S_{2Mo}$  in Figure 2D (Supporting Information Figure S4 shows the band structures for all the point defects). While  $S_{2Mo}$  with relatively low formation energy under S-rich conditions only has occupied deep levels, both  $V_S$  and  $V_{S_2}$  introduce two unoccupied deep levels about 0.6 eV below the conduction bands minimum (CBM). The deep levels below the CBM for the  $V_S$  and  $V_{S_2}$  vacancies might make them act as compensation centers in *n*-type MoS<sub>2</sub>. The theoretical results are consistent with the experimental observations of enhanced conductance after S annealing,<sup>10</sup> which would decrease the concentration of S vacancies. Yet, further theoretical and experimental efforts are needed to fully understand the origin of the omnipresent *n*-type conductivity in CVD grown MoS<sub>2</sub>.<sup>2,3,7,10</sup>

Although the electron beam energy is much lower than the knock-on damage threshold calculated for MoS<sub>2</sub>,<sup>19</sup> defects can



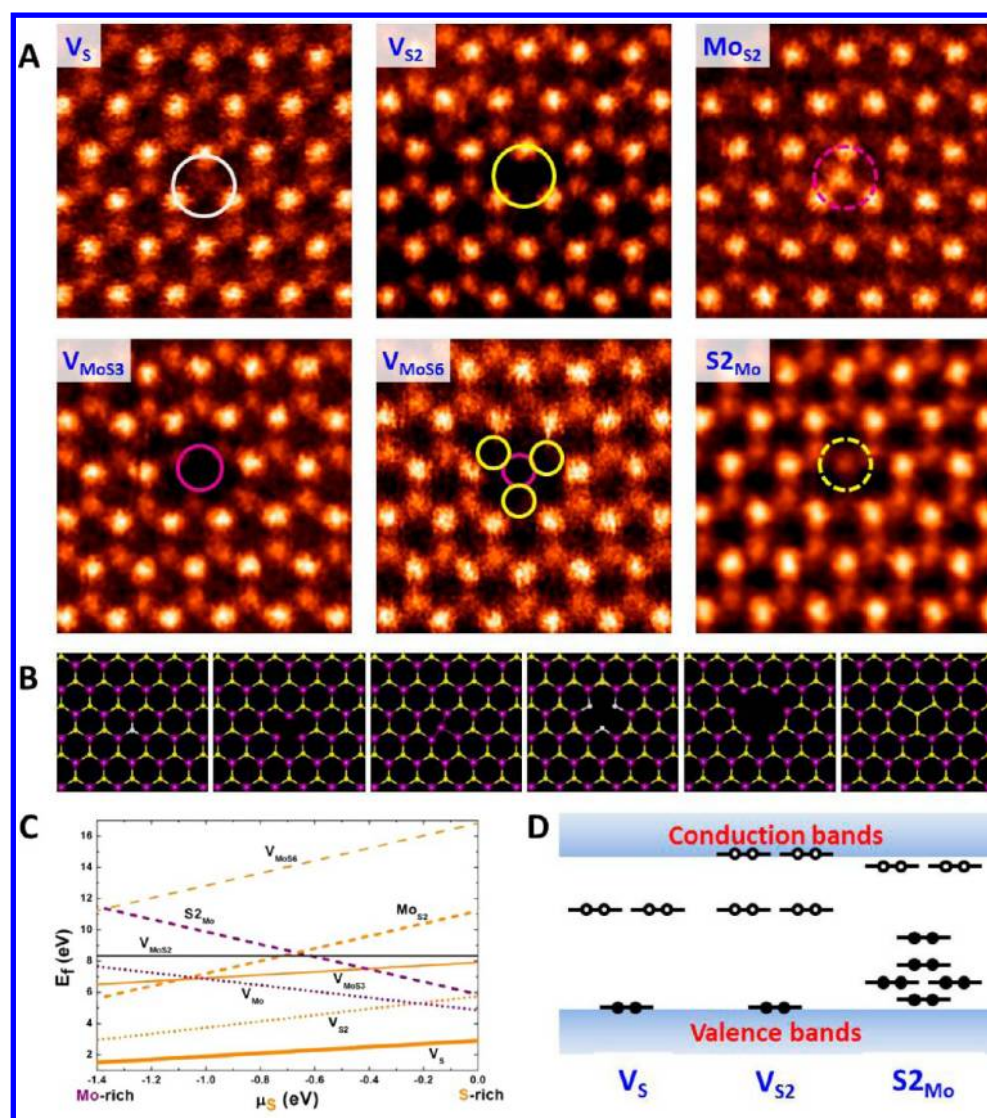


**Figure 2.** Intrinsic point defects in monolayer MoS<sub>2</sub>. (A) Atomic resolution ADF images of various intrinsic point defects present in monolayer CVD MoS<sub>2</sub>, including V<sub>S</sub>, V<sub>S2</sub>, Mo<sub>S2</sub>, V<sub>MoS3</sub>, V<sub>MoS6</sub>, and S<sub>2</sub>Mo. (B) Fully relaxed structural models of the six types of point defects observed experimentally. From left to right: V<sub>S</sub>, V<sub>S2</sub>, Mo<sub>S2</sub>, V<sub>MoS3</sub>, V<sub>MoS6</sub>, and S<sub>2</sub>Mo. Purple, yellow, and white balls represent Mo, top layer S, and bottom layer S, respectively. (C) Formation energies of different point defects as functions of sulfur chemical potential, plotted in the range  $-1.4 \text{ eV} < \mu_S < 0 \text{ eV}$ , where MoS<sub>2</sub> can remain stable with respect to the formation of bulk Mo ( $\mu_S = -1.4 \text{ eV}$ ) or bulk alpha-S ( $\mu_S = 0 \text{ eV}$ ). (D) Schematic representation of the defect levels.

still be generated in the sample under extended electron irradiation, presumably via ionization damage and/or catalyzed by hydrocarbon surface contamination. Interestingly, we find that extended electron irradiation preferentially generates two types of defects: V<sub>S</sub> and V<sub>MoS3</sub>, as shown in Supporting Information Figure S5. The result provides an alternative way to control the concentration of these two types of defects in monolayer MoS<sub>2</sub>. Moreover, because such vacancy generation is mainly via ionization damage instead of knock-on damage, in principle the modification can be performed even in a regular scanning electron microscopy (SEM) under 30 kV, readily accessible in most research laboratories. The preferential generation of V<sub>MoS3</sub> under electron irradiation could potentially be useful for chemical sensing<sup>26</sup> and hydrogen generation,<sup>27,28</sup> utilizing active edge sites.<sup>27</sup> Moreover, filling the metal vacancy complexes with foreign atoms, such as other transition metals, provides new opportunities to tune the magnetic properties of

the MoS<sub>2</sub> and may generate a new family of 2D dilute magnetic semiconductors.

Besides the vacancies and antisite defects, adatoms of Mo and S were also frequently observed at various sites on CVD-grown MoS<sub>2</sub> samples as shown in Supporting Information Figure S6. The direct observation of various point defects in monolayer MoS<sub>2</sub> provides clues to the performance of MoS<sub>2</sub> materials. Moreover, the concentration of various defects can be controlled to a certain extent by regulating the synthesis process or deliberately induced via irradiation by high energy particles, including electron beam, ion beam,<sup>29</sup> high energy laser, or by chemical etching,<sup>30,31</sup> providing flexibility to tune the performance of the material for specific applications.

The peculiar bonding characteristics between Mo and S in monolayer MoS<sub>2</sub> render a variety of dislocation cores, including not only the topologically conventional one with five- and 7-fold (S17) rings, but also new core structures with 4/4, 4/6, 4/8, and 6/8 fold rings that compose various grain boundaries (GBs)

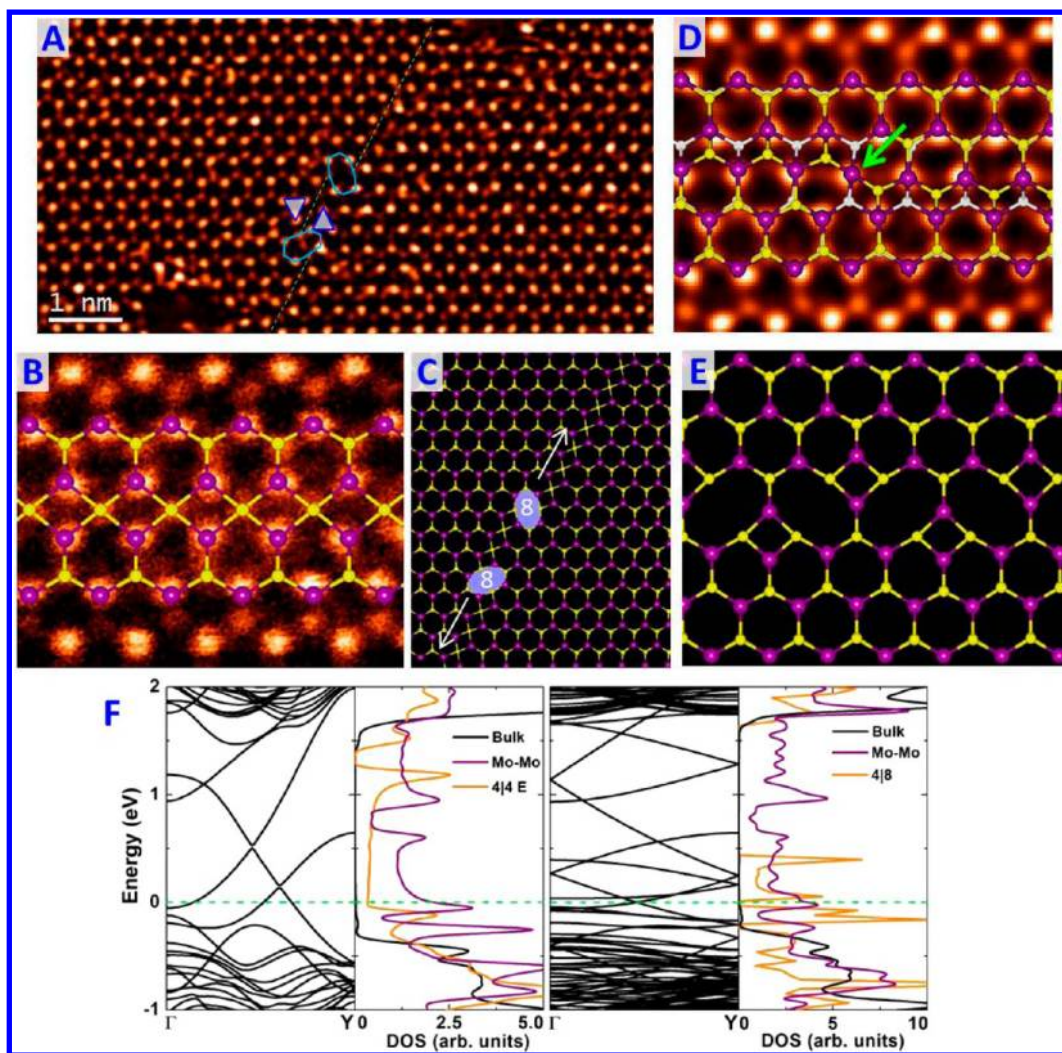


**Figure 3.** Atomic structure of  $60^\circ$  grain boundaries in monolayer  $\text{MoS}_2$ . (A) ADF image of a 4l4P  $60^\circ$  grain boundary. The green dash line highlights the position of the 4l4P grain boundary, and the grain boundary steps are linked by octagons as indicated. The blue triangles illustrate the orientation of the two grains with  $60^\circ$  rotation. (B) ADF image of the 4l4P  $60^\circ$  GB structures with the structural model overlaid. (C) Schematic structure of the GB and GB kinks as shown in panel A. (D) ADF image and overlaid structural model of a 4l4E type  $60^\circ$  grain boundary, and the grain boundary steps are linked by 4-fold coordinated Mo atoms as highlighted. (E) Relaxed structure for 4l8 GB, representing a 4l4P GB with the highest kink density. (F) Band structures and local density of states (LDOS) of the 4l4E and 4l8 GBs.

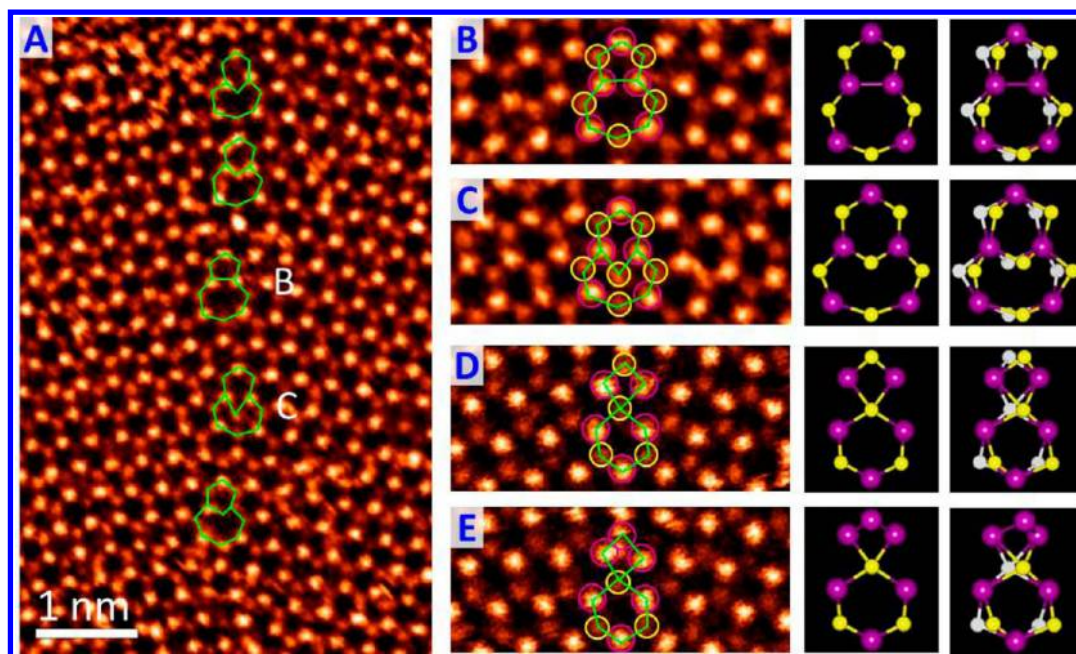
as predicted by theory.<sup>18</sup> However, these new GB structures have never been observed experimentally. Using atomic-resolution STEM-ADF imaging, we report a comprehensive study of various dislocation core structures that constitute the GBs in  $\text{MoS}_2$ , which are distinctly different from GBs in graphene.

Figure 3A shows a  $60^\circ$  GB in  $\text{MoS}_2$ . The GB is parallel to the zigzag direction of the  $\text{MoS}_2$  lattice and is composed of 4-fold rings with point sharing at a common S2 site (denoted as 4l4P structure). The structure of the 4l4P type GB is clearly shown in Figure 3B with the relaxed structure model overlaid. The Mo atoms at this GB retain the regular 6-fold coordination; however, the S atoms at the GB change from the regular 3-fold coordination to 4-fold coordination, a phenomenon that has not been observed in graphene GBs. More importantly, this particular GB structure was predicted to serve as a perfect 1D metallic stripe embedded in the otherwise semiconducting  $\text{MoS}_2$ ,<sup>18</sup> which could provide new functionalities and form intrinsic electronic heterostructures in monolayer  $\text{MoS}_2$ .

It is well-known that GBs are usually not perfectly straight and are linked by various GB kinks that can have important influences on the material properties.<sup>32</sup> As can be seen from Figure 3A and Supporting Information Figure S7, the GB indeed contains a few parallel displaced 4l4P segments linked by two octagonal kinks. The separation of these kinks (white arrows in Figure 3C) generates 4l4P segments with different lengths, providing the general description of this particular type of  $60^\circ$  GB in monolayer  $\text{MoS}_2$ . Sometimes S atoms can be adsorbed inside the 8-fold rings due to the large space available, making it resemble two distorted hexagons (bottom kink in Figure 3A).

Depending on the precise manner how the two  $60^\circ$  rotated grains meet, another type of  $60^\circ$  GB consisting of strings of 4-fold rings with edge sharing (4l4E) can also form, as shown in Figure 3D, which has not been predicted by previous theoretical studies. In this case, the two grains are shifted by half of the primitive lattice vector along the GB. STEM-ADF image analysis shows that the S sites along the GB are occupied by monosulfur atoms, that is, 50% S coverage, generating bonds





**Figure 4.** Atomic structure of small-angle grain boundaries in monolayer  $\text{MoS}_2$ . (A–C) STEM-ADF images of an  $18.5^\circ$  grain boundary consisting of dislocations with five- and seven-fold rings (5/7) and dislocations with six- and eight-fold rings (6/8). Panels B and C are the zoom-in view of the 5/7 and 6/8 structures from the regions indicated in A. (D,E) ADF images of a  $17.5^\circ$  grain boundary consisting of dislocations with four- and six-fold rings (4/6), either pristine (D) or with Mo-substitution (E). The 2D and 3D structural models for the various dislocation structures are placed next to the corresponding ADF images.

between the S atoms from one grain and Mo atoms from the other. The 4/4E GB with 50% S coverage renders 5- and 3-fold coordination for Mo and S atoms at the GB, respectively, a decrease in coordination for Mo. As confirmed by DFT calculations, the energy of 4/4E GB with 50% S coverage is about  $0.1 \text{ eV/\AA}$  lower than that with full S coverage, even under S-rich conditions. Moreover, the 4/4E GBs have the same local stoichiometry as the energy-favorable 4/4P structure, and the energy difference is only  $0.04 \text{ eV/\AA}$ . Similar to the 4/4P GBs, GB kinks were also observed in the 4/4E GB. As highlighted in Figure 3D, the 4/4E GBs are linked by a 4-fold coordinated Mo, a further decrease in coordination for Mo.

We then explore the electronic structures of the experimentally observed GBs using DFT calculations. Figure 3F shows the band structure and local density of states (LDOS) for the 4/4E GB. Similar to the 4/4P GBs, 4/4E GBs also serve as perfect 1D metallic quantum wires embedded in the semiconducting  $\text{MoS}_2$  matrix with dispersive bands crossing the Fermi level. The states near the Fermi level, delocalized in one dimension, are visualized through the partial charge density (Supporting Information Figure S8). While the perfect metallicity is present in ideal 4/4P or 4/4E GBs, kinks can induce significant disturbance to the electronic behavior of the GBs. Here, we consider an extreme case, corresponding to a 4/4P GB with the highest density of kink pairs, which essentially is a line of 4/8s (4/8 GB) as shown in Figure 3E. Interestingly, in sharp contrast to 4/4P GB, 4/8 GB only introduces localized midgap states right above the top of valence bands of the  $\text{MoS}_2$  matrix, as demonstrated by comparing the LDOS and bandstructure in Figure 3F. This clearly shows the influences of the octagonal kinks on the electronic properties of the metallic 4/4P GB.

Besides the mirror-symmetric 4/4P and 4/4E  $60^\circ$  GBs, we also explore other possible GB configurations with smaller tilt angles. Figure 4A shows an  $18.5^\circ$  GB composed of 5/7 and 6/8

structures as schematically shown in the STEM-ADF image. The detailed atomic structures for the 5/7 and 6/8 dislocation cores are shown in Figure 4B,C, respectively. The 5/7 structure can serve as the basic dislocation core structure, and the addition of monosulfur or disulfur into the Mo–Mo bonds generates the 6/8 structures observed at the same GB. As has been shown by calculations,<sup>18</sup> such a transition is energetically favorable only under S-rich conditions, suggesting that the GB observed in Figure 4A with high density of 6/8 structures may be grown under a S-rich local environment. However, a different GB observed in another area of the continuous  $\text{MoS}_2$  film shows primarily 4/6 structures (Figure 4D,E) with 4- and 6-fold rings joined by 4-fold coordinated S atoms. The pristine 4/6 structure (Figure 4D) can be derived from S-oriented 5/7 structures by removing 2 S atoms (Supporting Information Figure S9), which is energetically favorable under Mo-rich conditions.<sup>18</sup> Moreover, our calculations show that Mo substitution in the 4/6 structure has a formation energy  $3.2 \text{ eV}$  lower than that of  $\text{MoS}_2$  in a perfect  $\text{MoS}_2$  matrix. On the basis of the energy landscape, the 4/6 and Mo-substituted 4/6 GBs are most likely formed under Mo-rich local environments. The coexistence of S-rich and Mo-rich GBs in the same CVD grown  $\text{MoS}_2$  film thus indicates the local fluctuation of Mo and S source concentrations during material growth, calling for a further refinement of the synthesis method. The richness in dislocation core and GB structures and enhanced interaction of GBs with point defects also suggest exciting possibilities of controlling the precise GB structures and thus the local properties of GB via fine-tuning the chemical environment during growth.

Finally, we touch on a distinct edge reconstruction in monolayer  $\text{MoS}_2$ , which is captured as a transition state during material growth. As previously shown by optical micrographs,<sup>11</sup>  $\text{MoS}_2$  crystals tend to have very regular orientations and shapes, and thus the idealized edge structure can be estimated from the

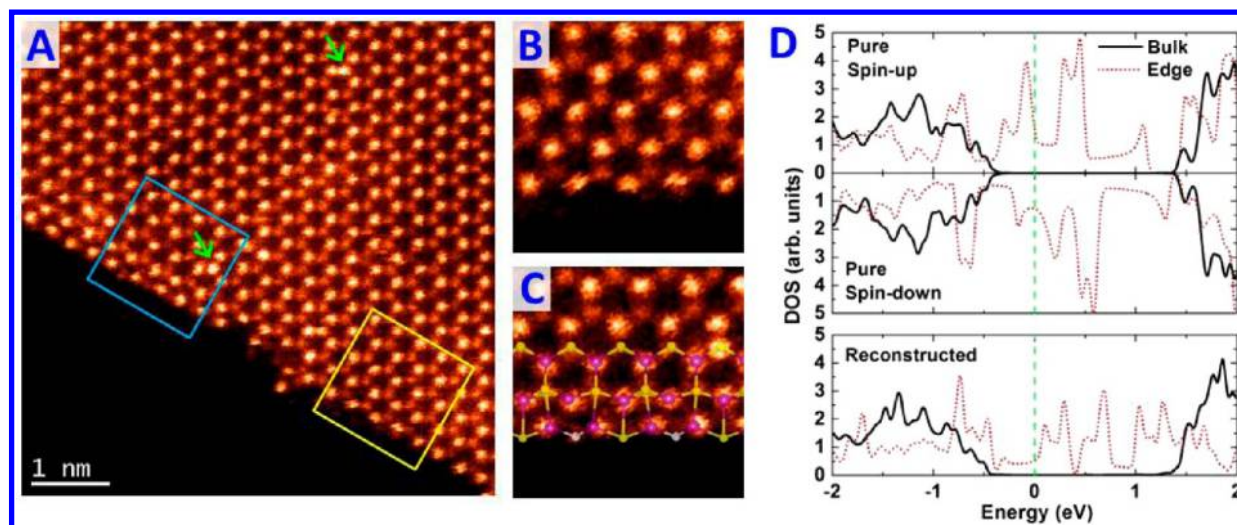


**Figure 5.** Edge reconstruction in monolayer MoS<sub>2</sub> as a transition state during CVD growth. (A) ADF image of a Mo-terminated edge. The green arrows highlight the presence of Mo adatoms on S sites. (B) Zoom-in view of the region highlighted by the yellow square in A, showing the regular Mo-terminated edge. (C) Zoom-in view of the region highlighted by the blue square in A with relaxed structural model overlaid, showing reconstruction of the Mo-terminated edge due to sulfur deficiency during growth. The edge Mo atoms are pulled closer to the center of the 6-fold rings as compared with the regular Mo-terminated edge. The S atoms at the reconstructed edge are monosulfur instead of disulfur, that is, containing V<sub>S</sub>. (D) Local density of states (LDOS) for pure and reconstructed edges.

orientation and crystal shape of the MoS<sub>2</sub> patch.<sup>33</sup> However, such estimation only provides a macroscale picture of the edges, and the precise atomic-scale structural information in particular for edge reconstructions still requires atomic resolution imaging.<sup>34–37</sup> An example is shown in Supporting Information Figure S10 where the edge is not straight at the nanometer scale and contains many atomic steps. The step edges provide additional Mo and S sites with unsaturated bonds, which could potentially be useful in catalytic applications.<sup>35,38</sup> Even at the straight segments of the Mo-terminated edge, two different types of atomic configurations can often be observed: namely the regular Mo-edge with bare Mo termination, and the 50% S-covered Mo-edge with one additional S atom for each Mo atom on the edge, as shown in Supporting Information Figure S11. Although the 50% S-covered Mo-edge is predicted to be energetically stable compared to regular Mo-edge under the thermodynamic range of the S chemical potential,<sup>33</sup> the frequently observed regular Mo-edge highlights the non-equilibrium environment during the growth process.

In addition to the low-energy Mo-terminated and 50% S-covered edges, a new type of edge reconstruction was observed, presumably formed under a Mo-rich growth environment. As shown in Figure 5A, the lower part of the edge has the regular Mo-terminated structure (Figure 5B), while on the upper part, the outmost row of Mo atoms undergo a strong reconstruction, moving closer to the inner Mo row. The detailed atomic structure of the reconstructed edge is shown in Figure 5C with the relaxed structural model from DFT calculations overlaid. Image analysis shows that the S atoms at this reconstructed edge are monosulfur, that is, containing 50% of S vacancies. The presence of an array of V<sub>S</sub> along the Mo edges induces the observed reconstruction and enhances the interaction between the two outermost rows of Mo atoms. Furthermore, we find that this type of Mo-rich reconstructed edge can form under Mo-rich or S-deficient conditions (Supporting Information Figure S12), representing a transition state of the edge during growth. The theoretical prediction is supported by the observation of Mo adatoms near the reconstructed edge

(Figure 5A), indicating a Mo-rich local environment. Continuous supply of S during high-temperature growth would restore the reconstructed edge back to the regular Mo-terminated edge shown in Figure 5B and Supporting Information Figure S11.

Since the reconstructed edge can form during growth, it is of particular interest to investigate its electronic structure. It has been shown that the bare Mo-terminated edge has a ferromagnetic ground state,<sup>39</sup> which is also confirmed by our spin-polarized calculations (about 30 meV energy drop per edge Mo atom). As shown in Figure 5D, the LDOS for the unreconstructed Mo-terminated edge shows asymmetry between spin-up and spin-down channels, and every edge Mo atom possesses a local magnetic moment as high as 0.4  $\mu_B$ . In contrast, the Mo magnetic moments are totally quenched in the reconstructed Mo edges, while the metallic behavior of the edge is still well-preserved.

Using atomic-resolution direct imaging, the presence of various intrinsic point defects, including vacancies, vacancy complexes, antisite defects and adatoms, has been experimentally identified. Grain boundary structures are shown to be more complex than those in graphene, containing 4/4, 5/7, 6/8, and 4/6 dislocation core structures that extend three-dimensionally. The unexpected observation of metallic behaviors in all straight 60° GBs suggests the potential construction of electronic heterostructures at such interfaces by pattern growth of faceted MoS<sub>2</sub> grains with mirror symmetry. The reconstructed edge generated as a transition state during growth implies that new types of edges could be obtained by carefully controlling the local chemical environment during the synthesis, which may have interesting new applications in heterogeneous catalysis. The preferential generation of specific types of vacancies and vacancy complexes under electron beam irradiation and the enhanced interaction of impurities at defect sites offer an alternative way to dope this material via a sputtering-filling process and provides new opportunities to tune the material properties for more diversified applications by taking advantage of these structural defects.



The comprehensive study of different intrinsic structural defects in MoS<sub>2</sub> presented in this paper provides new insights into how the growth conditions affect the defect formation and how these structural defects could influence the properties of the material. Since all layered transition-metal dichalcogenides have very similar structures, the structural defects observed in this study are expected to be present in other 2D transition-metal dichalcogenides. The knowledge developed in this study could help to refine the synthesis strategies and to optimize the performance of 2D transition-metal dichalcogenides in general.

## ■ ASSOCIATED CONTENT

### Supporting Information

Description of the methods for MoS<sub>2</sub> growth, TEM sample preparation, microscopy characterization, and density functional calculations, as well as supplementary figures. This material is available free of charge via the Internet at <http://pubs.acs.org>.

## ■ AUTHOR INFORMATION

### Corresponding Author

\*E-mail: [zhouw1@ornl.gov](mailto:zhouw1@ornl.gov).

### Author Contributions

W.Z. carried out the electron microscopy experiments, and performed the data analysis. X.Z. performed the DFT calculations and analyzed the data under the supervision of B.I.Y. The MoS<sub>2</sub> TEM samples used for collecting the data shown in the manuscript were grown and prepared by S.N. and Z.L. under the supervision of J.L. and P.M.A. The initial MoS<sub>2</sub> samples used for preliminary experiments were grown and prepared by Y.S. and J.K. J.C.L., B.I.Y., J.L., and P.M.A. advised on data analysis and supervised the project. W.Z. and X.Z. wrote the paper. All authors helped with data analysis and manuscript preparation.

W.Z. and X.Z. contributed equally to this work.

### Notes

The authors declare no competing financial interest.

## ■ ACKNOWLEDGMENTS

This research was supported in part by National Science Foundation through Grant DMR-0938330 and a Wigner Fellowship through the Laboratory Directed Research and Development Program of Oak Ridge National Laboratory, managed by UT-Battelle, LLC, for the U.S. Department of Energy (W.Z.); Oak Ridge National Laboratory's Shared Research Equipment (ShaRE) User Facility Program (JCI), which is sponsored by the Office of Basic Energy Sciences, U.S. Department of Energy; the Welch Foundation Grant C-1716, the NSF Grant DMR-0928297, the U.S. Army Research Office MURI Grant W911NF-11-1-0362, the U.S. Office of Naval Research MURI Grant N00014-09-1-1066, and the Nanoelectronics Research Corporation contract S201006. The computations were performed at the Cyberinfrastructure for Computational Research funded by NSF under Grant CNS-0821727 and the Data Analysis and Visualization Cyberinfrastructure funded by NSF under Grant OCI-0959097. Y.S. and J.K. acknowledge the support from NSF DMR 0845358.

## ■ REFERENCES

- (1) Mak, K. F.; Lee, C.; Hone, J.; Shan, J.; Heinz, T. F. Atomically Thin MoS<sub>2</sub>: A New Direct-Gap Semiconductor. *Phys. Rev. Lett.* **2010**, *105*, 136805.
- (2) Radisavljevic, B.; Radenovic, A.; Brivio, J.; Giacometti, V.; Kis, A. Single-Layer MoS<sub>2</sub> Transistors. *Nat. Nanotechnol.* **2011**, *6*, 147–150.
- (3) Yin, Z.; Li, H.; Li, H.; Jiang, L.; Shi, Y.; Sun, Y.; Lu, G.; Zhang, Q.; Chen, X.; Zhang, H. Single-Layer MoS<sub>2</sub> Phototransistors. *ACS Nano* **2011**, *6*, 74–80.
- (4) Zeng, Z.; Yin, Z.; Huang, X.; Li, H.; He, Q.; Lu, G.; Boey, F.; Zhang, H. Single-Layer Semiconducting Nanosheets: High-Yield Preparation and Device Fabrication. *Angew. Chem., Int. Ed.* **2011**, *50*, 11093–11097.
- (5) Wang, Q. H.; Kalantar-Zadeh, K.; Kis, A.; Coleman, J. N.; Strano, M. S. Electronics and Optoelectronics of Two-Dimensional Transition Metal Dichalcogenides. *Nat. Nanotechnol.* **2012**, *7*, 699–712.
- (6) Mak, K. F.; He, K.; Shan, J.; Heinz, T. F. Control of Valley Polarization in Monolayer MoS<sub>2</sub> by Optical Helicity. *Nat. Nanotechnol.* **2012**, *7*, 494–498.
- (7) Lee, Y.-H.; Zhang, X.-Q.; Zhang, W.; Chang, M.-T.; Lin, C.-T.; Chang, K.-D.; Yu, Y.-C.; Wang, J. T.-W.; Chang, C.-S.; Li, L.-J.; Lin, T.-W. Synthesis of Large-Area MoS<sub>2</sub> Atomic Layers with Chemical Vapor Deposition. *Adv. Mater.* **2012**, *24*, 2320–2325.
- (8) Zhan, Y.; Liu, Z.; Najmaei, S.; Ajayan, P. M.; Lou, J. Large-Area Vapor-Phase Growth and Characterization of MoS<sub>2</sub> Atomic Layers on a SiO<sub>2</sub> Substrate. *Small* **2012**, *8*, 966–971.
- (9) Shi, Y.; Zhou, W.; Lu, A.-Y.; Fang, W.; Lee, Y.-H.; Hsu, A. L.; Kim, S. M.; Kim, K. K.; Yang, H. Y.; Li, L.-J.; Idrobo, J.-C.; Kong, J. van der Waals epitaxy of MoS<sub>2</sub> Layers Using Graphene As Growth Templates. *Nano Lett.* **2012**, *12*, 2784–2791.
- (10) Liu, K.-K.; Zhang, W.; Lee, Y.-H.; Lin, Y.-C.; Chang, M.-T.; Su, C.-Y.; Chang, C.-S.; Li, H.; Shi, Y.; Zhang, H.; Lai, C.-S.; Li, L.-J. Growth of Large-Area and Highly Crystalline MoS<sub>2</sub> Thin Layers on Insulating Substrates. *Nano Lett.* **2012**, *12*, 1538–1544.
- (11) Najmaei, S.; Liu, Z.; Zhou, W.; Zou, X.; Shi, G.; Lei, S.; Yakobson, B. I.; Idrobo, J. C.; Ajayan, P. M.; Lou, J. Vapor Phase Growth and Grain Boundary Structure of Molybdenum Disulfide Atomic Layers. 2013, arXiv:1301.2812 (accessed Jan 13, 2013).
- (12) Banhart, F.; Kotakoski, J.; Krasheninnikov, A. V. Structural Defects in Graphene. *ACS Nano* **2011**, *5*, 26–41.
- (13) Wei, Y.; Wu, J.; Yin, H.; Shi, X.; Yang, R.; Dresselhaus, M. D. The Nature of Strength Enhancement and Weakening by Pentagon–Heptagon Defects in Graphene. *Nat. Mater.* **2012**, *11*, 759–763.
- (14) Yu, Q.; Jauregui, L. A.; Wu, W.; Colby, R.; Tian, J.; Su, Z.; Cao, H.; Liu, Z.; Pandey, D.; Wei, D.; Chung, T. F.; Peng, P.; Guisinger, N. P.; Stach, E. A.; Bao, J.; Pei, S.-S.; Chen, Y. P. Control and Characterization of Individual Grains and Grain Boundaries in Graphene Grown by Chemical Vapour Deposition. *Nat. Mater.* **2011**, *10*, 443–449.
- (15) Yazyev, O. V.; Louie, S. G. Electronic Transport in Polycrystalline Graphene. *Nat. Mater.* **2010**, *9*, 806–809.
- (16) Chen, J.-H.; Li, L.; Cullen, W. G.; Williams, E. D.; Fuhrer, M. S. Tunable Kondo Effect in Graphene with Defects. *Nat. Phys.* **2011**, *7*, 535–538.
- (17) Zhou, W.; Pennycook, S. J.; Idrobo, J.-C. Localization of Inelastic Electron Scattering in the Low-Loss Energy Regime. *Ultramicroscopy* **2012**, *119*, 51–56.
- (18) Zou, X.; Liu, Y.; Yakobson, B. I. Predicting Dislocations and Grain Boundaries in Two-Dimensional Metal-Disulfides from the First Principles. *Nano Lett.* **2013**, *13*, 253–258.
- (19) Komsa, H.-P.; Kotakoski, J.; Kurasch, S.; Lehtinen, O.; Kaiser, U.; Krasheninnikov, A. V. Two-Dimensional Transition Metal Dichalcogenides under Electron Irradiation: Defect Production and Doping. *Phys. Rev. Lett.* **2012**, *109*, 035503.
- (20) van der Zande, A. M.; Huang, P. Y.; Chenet, D. A.; Berkelbach, T. C.; You, Y.; Lee, G.-H.; Heinz, T. F.; Reichman, D. R.; Muller, D. A.; Hone, J. C. Grains and Grain Boundaries in Highly Crystalline Monolayer Molybdenum Disulfide. 2013, arXiv:1301.1985 (accessed Jan 13, 2013).
- (21) Krivanek, O. L.; Chisholm, M. F.; Nicolosi, V.; Pennycook, T. J.; Corbin, G. J.; Dellby, N.; Murfitt, M. F.; Own, C. S.; Szilagy, Z. S.; Oxley, M. P.; Pantelides, S. T.; Pennycook, S. J. Atom-by-Atom

Structural and Chemical Analysis by Annular Dark-Field Electron Microscopy. *Nature* **2010**, 464, 571–574.

(22) Zhou, W.; Oxley, M. P.; Lupini, A. R.; Krivanek, O. L.; Pennycook, S. J.; Idrobo, J. C. Single Atom Microscopy. *Microsc. Microanal.* **2012**, 18, 1342–1354.

(23) Dumcenco, D. O.; Kobayashi, H.; Liu, Z.; Huang, Y.-S.; Suenaga, K. Visualization and Quantification of Transition Metal Atomic Mixing in  $\text{Mo}_{1-x}\text{W}_x\text{S}_2$  Single Layers. *Nat. Commun.* **2013**, 4, 1351.

(24) Krasheninnikov, A. V.; Lehtinen, P. O.; Foster, A. S.; Nieminen, R. M. Bending the Rules: Contrasting Vacancy Energetics and Migration in Graphite and Carbon Nanotubes. *Chem. Phys. Lett.* **2006**, 418, 132–136.

(25) Lee, G. D.; Wang, C. Z.; Yoon, E.; Hwang, N. M.; Kim, D. Y.; Ho, K. M. Diffusion, Coalescence, and Reconstruction of Vacancy Defects in Graphene Layers. *Phys. Rev. Lett.* **2005**, 95, 205501.

(26) Li, H.; Yin, Z. Y.; He, Q. Y.; Li, H.; Huang, X.; Lu, G.; Fam, D. W. H.; Tok, A. I. Y.; Zhang, Q.; Zhang, H. Fabrication of Single- and Multilayer  $\text{MoS}_2$  Film-Based Field-Effect Transistors for Sensing NO at Room Temperature. *Small* **2012**, 8, 63–67.

(27) Hinnemann, B.; Moses, P. G.; Bonde, J.; Jorgensen, K. P.; Nielsen, J. H.; Horch, S.; Chorkendorff, I.; Nørskov, J. K. Biomimetic Hydrogen Evolution:  $\text{MoS}_2$  Nanoparticles As Catalyst for Hydrogen Evolution. *J. Am. Chem. Soc.* **2005**, 127, 5308–5309.

(28) Ataca, C.; Ciraci, S. Dissociation of  $\text{H}_2\text{O}$  at the Vacancies of Single-Layer  $\text{MoS}_2$ . *Phys. Rev. B* **2012**, 85, 195410.

(29) Krasheninnikov, A. V.; Nordlund, K. Ion and Electron Irradiation-Induced Effects in Nanostructured Materials. *J. Appl. Phys.* **2010**, 107, 071301.

(30) Xie, L.; Jiao, L.; Dai, H. Selective Etching of Graphene Edges by Hydrogen Plasma. *J. Am. Chem. Soc.* **2010**, 132, 14751–14753.

(31) Wang, X.; Dai, H. Etching and Narrowing of Graphene from the Edges. *Nature Chem.* **2010**, 2, 661–665.

(32) Hirth, J. P.; Lothe, J. *Theory of dislocations*, 2nd ed.; Wiley: New York, 1982.

(33) Schweiger, H.; Raybaud, P.; Kresse, G.; Toulhoat, H. Shape and Edge Sites Modifications of  $\text{MoS}_2$  Catalytic Nanoparticles Induced by Working Conditions: A Theoretical Study. *J. Catal.* **2002**, 207, 76–87.

(34) Helveg, S.; Lauritsen, J. V.; Laegsgaard, E.; Stensgaard, I.; Nørskov, J. K.; Clausen, B. S.; Topsøe, H.; Besenbacher, F. Atomic-Scale Structure of Single-Layer  $\text{MoS}_2$  Nanoclusters. *Phys. Rev. Lett.* **2000**, 84, 951–954.

(35) Lauritsen, J. V.; Kibsgaard, J.; Helveg, S.; Topsøe, H.; Clausen, B. S.; Laegsgaard, E.; Besenbacher, F. Size-Dependent Structure of  $\text{MoS}_2$  Nanocrystals. *Nat. Nanotechnol.* **2007**, 2, 53–58.

(36) Hansen, L. P.; Ramasse, Q. M.; Kisielowski, C.; Brorson, M.; Johnson, E.; Topsøe, H.; Helveg, S. Atomic-Scale Edge Structures on Industrial-Style  $\text{MoS}_2$  Nanocatalysts. *Angew. Chem., Int. Ed.* **2011**, 50, 10153–10156.

(37) Liu, Z.; Suenaga, K.; Wang, Z.; Shi, Z.; Okunishi, E.; Iijima, S. Identification of Active Atomic Defects in a Monolayered Tungsten Disulphide Nanoribbon. *Nat. Commun.* **2011**, 2, 213.

(38) Gemming, S.; Seifert, G. Nanocrystals - Catalysts on the Edge. *Nat. Nanotechnol.* **2007**, 2, 21–22.

(39) Li, Y.; Zhou, Z.; Zhang, S.; Chen, Z.  $\text{MoS}_2$  Nanoribbons: High Stability and Unusual Electronic and Magnetic Properties. *J. Am. Chem. Soc.* **2008**, 130, 16739–16744.